



Empirical Measurement of the Dynamical Ages of Three Globular Clusters and Some Considerations on the Use of the Dynamical Clock*

Francesco R. Ferraro^{1,2} , Barbara Lanzoni^{1,2} , Enrico Vesperini³ , Mario Cadelano^{1,2} , Dan Deras¹ , and Cristina Pallaanca^{1,2}

¹ Dipartimento di Fisica e Astronomia, Università di Bologna, Via Gobetti 93/2, I-40129 Bologna, Italy; francesco.ferraro3@unibo.it

² INAF—Osservatorio di Astrofisica e Scienze dello Spazio di Bologna, Via Gobetti 93/3, I-40129 Bologna, Italy

³ Department of Astronomy, Indiana University, Bloomington, IN 47401, USA

Received 2023 February 13; revised 2023 April 13; accepted 2023 April 14; published 2023 June 19

Abstract

We have used the “dynamical clock” to measure the level of dynamical evolution reached by three Galactic globular clusters (namely, NGC 3201, NGC 6316, and NGC 6440). This is an empirical method that quantifies the level of central segregation of blue straggler stars (BSSs) within the cluster half-mass radius by means of the A_{rh}^+ parameter, defined as the area enclosed between the cumulative radial distribution of BSSs and that of a lighter population. The total sample with homogeneous determinations of A_{rh}^+ currently includes 59 clusters: 52 old GCs in the Milky Way (including the three investigated here), five old clusters in the Large Magellanic Cloud, and two young systems in the Small Magellanic Cloud. The three objects studied here nicely nest into the correlation between A_{rh}^+ and the central relaxation time defined by the previous sample, thus proving and consolidating the use of the dynamical clock as an excellent tracer of the stage of dynamical evolution of a star cluster in different galactic environments. Finally, we discuss the advantages of using the dynamical clock as an indicator of the dynamical ages of star clusters, compared to the present-day central relaxation time.

Unified Astronomy Thesaurus concepts: Globular star clusters (656); Blue straggler stars (168); Photometry (1234)

1. Introduction

Globular clusters (GCs) are the prototypes of “collisional stellar systems” in the universe. Recurrent gravitational interactions among their constituent stars favor continuous exchanges of kinetic energy driving the system toward energy equipartition and inducing severe perturbations to the stellar orbits. Heavy stars tend to progressively sink toward the central region of the cluster (due to dynamical friction), while low-mass stars migrate outward and can even escape from the (mass-segregated) system. The redistribution of kinetic energy tends to completely erase the initial kinematic and structural conditions, bringing the cluster toward a (quasi-)thermodynamically relaxed state (see, e.g., Trenti & van der Marel 2013; Bianchini et al. 2016) on a characteristic timescale that can be significantly shorter than its age. The relaxation time depends in a very complex way on the initial and local conditions, and thus differs from cluster to cluster and, within the same system, from high- to low-density regions (e.g., Meylan & Heggie 1997). Thus, even clusters formed at the same epoch (i.e., with the same chronological age) are expected to show different levels of dynamical evolution (namely, different dynamical ages). The macroscopic manifestation of internal changes induced by the dynamical evolution of the system is a progressive contraction of the central regions (in particular, of the core radius, r_c) and a corresponding increase in the central density (ρ_0) virtually up to infinity, in a runaway process that is

called “core collapse” and is thought to be halted by the formation and hardening of binary systems (e.g., Meylan & Heggie 1997). However, an opposite behavior, where the core radius progressively expands with time due to the heating effect of a retained population of stellar-mass black holes, has been advocated (Mackey et al. 2008) to explain the size–age conundrum observed in the Magellanic Clouds, where young star clusters are all compact while the old ones show both small and large core sizes (Mackey & Gilmore 2003a, 2003b). This indicates how difficult and uncertain it is to estimate the dynamical age of stellar systems solely from measuring their structural parameters, and clearly calls for additional methods providing a more direct empirical measure of the effects of the various processes driving the dynamical evolution of star clusters. Among these, the measurement of the stellar mass function, orbital anisotropy, and velocity dispersion profile at different radial distances or for groups with different stellar mass (e.g., Baumgardt & Makino 2003; Bianchini et al. 2016, 2018; Tiongco et al. 2016; Webb & Vesperini 2017; Cadelano et al. 2020a; Beccari et al. 2022) is still quite challenging for most GCs (e.g., Libralato et al. 2018, 2019; Cohen et al. 2021), while the study of special classes of heavy objects seems to be particularly promising. Indeed, the intense dynamical activity in GC interiors is thought to boost the formation of stellar exotica, such as blue straggler stars (BSSs) and binaries containing heavily degenerate objects, like black holes and neutron stars. Hence, on the one hand, the frequency and the properties of these exotica are expected to depend on the dynamical stage of the system, but on the other hand, the observational properties of this special class of objects can be used to get information on the internal dynamics of GCs (see, e.g., Pooley et al. 2003; Ransom et al. 2005; Ferraro et al. 2009, 2018a, 2019; Dalessandro et al. 2013; Verbunt & Freire 2014; Cadelano et al. 2017a, 2018, 2019, 2020b; Prager et al. 2017; Beccari et al. 2019).

* Based on observations collected at the Hubble Space Telescope, under proposals GO12517 (PI: Ferraro), GO13410 (PI: Pallaanca), GO15232 (PI: Ferraro).



Original content from this work may be used under the terms of the [Creative Commons Attribution 4.0 licence](https://creativecommons.org/licenses/by/4.0/). Any further distribution of this work must maintain attribution to the author(s) and the title of the work, journal citation and DOI.

Among the variety of exotica populating GC cores, BSSs are surely the most abundant and the easiest to distinguish from normal stars in a color–magnitude diagram (CMD), where they populate a sort of extension of the cluster main sequence (MS) toward brighter magnitudes and bluer colors than the MS turn-off (MS-TO) point (e.g., Sandage 1953; Ferraro et al. 1992, 1993, 1997, 1999a, 2003, 2006b; Piotto et al. 2004; Lanzoni et al. 2007a, 2007b, 2007c; Leigh et al. 2007; Dalessandro et al. 2008; Moretti et al. 2008; Beccari et al. 2011; Simunovic & Puzia 2016). Their “anomalous” location in the CMD suggests that BSSs are hydrogen-burning stars more massive than the others. The origin of such massive objects in stellar systems with no gas available for star formation requires the action of some mass-enhancement process. Two main BSS formation channels have been identified so far: mass transfer in binary systems (McCrea 1964), and stellar mergers resulting from direct collisions (Hills & Dale 1974; Sills et al. 2005). There is also growing observational evidence (Shara et al. 1997; Gilliland et al. 1998; Ferraro et al. 2006a; Fiorentino et al. 2014; Raso et al. 2019) confirming that they are indeed significantly heavier ($m_{\text{BSS}} = 1.2 M_{\odot}$) than the average cluster population ($\langle m \rangle = 0.3 M_{\odot}$). Hence, these objects represent powerful gravitational probes of processes that characterize the dynamical evolution of star clusters (e.g., Ferraro et al. 2009, 2012, 2018a, 2019; Lanzoni et al. 2016; Dresbach et al. 2022). Indeed, the signature of mass segregation and dynamical friction is expected to remain imprinted in some BSS observational properties, and in fact the radial distribution of these stars with respect to normal (lighter) cluster populations used as reference (REF) has been found to be a powerful (and fully empirical) indicator of the level of dynamical evolution reached by the host system, yielding the definition of the so-called “dynamical clock” (Ferraro et al. 2012). To solve complications related to the choice of radial binning, the original definition of the dynamical clock was later refined with the introduction of the A_{rh}^+ parameter (Alessandrini et al. 2016; Lanzoni et al. 2016; Ferraro et al. 2018a, 2020), which is the area enclosed between the cumulative radial distribution of BSSs and that of REF stars measured within the cluster half-mass radius (r_h). Hence, by construction, the A_{rh}^+ parameter quantifies the level of central segregation of BSSs with respect to the REF population, and it is expected to progressively increase with the dynamical aging of the host stellar system due to the more rapid sedimentation of heavier stars than of less massive objects. Large values of A_{rh}^+ are therefore expected for GCs in late stages of their dynamical evolution, while small values (down to zero) are predicted in dynamically young systems, where dynamical friction has not yet been effective in segregating BSSs toward the center. The A_{rh}^+ parameter therefore provides a direct, empirical measure of the central segregation of the heaviest observable stars within a cluster, as set by the combination of all the known (and still unknown) internal and external processes that drive mass segregation. In addition, it is defined within the half-mass radius, which is the physical length scale expected to vary the least during cluster dynamical evolution (see, e.g., Figure 4 in Bhat et al. 2022).

Indeed, a tight relation between A_{rh}^+ and the central relaxation time (t_{rc}) has been discovered for the Galactic GCs investigated so far (all sharing approximately the same chronological age), thus providing their direct ranking in terms

of dynamical age (Lanzoni et al. 2016; Ferraro et al. 2018a). The application of the dynamical clock to a sample of old star clusters in the Large Magellanic Cloud (LMC) has demonstrated that they follow the same relation defined by the Galactic ones (Ferraro et al. 2019). This has also contributed to clarifying the origin of the size–age conundrum, showing that the different core radii measured for the old GCs in the sample can be naturally explained by different dynamical ages (the dynamically older systems having smaller r_c than the younger clusters), with no need of a retained population of black holes. Ferraro et al. (2019) also pointed out that the distribution of the LMC clusters in the r_c –age diagram can in no way be interpreted as an evolutionary sequence because of the strong difference in mass between the young and the old clusters, which are less and more massive than $10^5 M_{\odot}$, respectively. Finally, Dresbach et al. (2022) recently demonstrated that the correlation found for the old GCs in the Galaxy and the LMC also holds for NGC 339 and NGC 419, two intermediate-age GCs in the Small Magellanic Cloud (SMC).

As part of the project “Cosmic-Lab,” which is aimed at using star clusters in the local universe as cosmic laboratories to study the complex interplay between the dynamical evolution of stellar systems and the photometric, kinematic, and chemical properties of their stellar populations (see, e.g., Lanzoni et al. 2010, 2013, 2016, 2019; Miocchi et al. 2013; Cadelano 2017b; Ferraro et al. 2018a, 2018b, 2019, 2020, 2021; Raso et al. 2019, 2020; Pallanca et al. 2021), here we study the BSS population and measure the A_{rh}^+ parameter in three additional Galactic GCs, namely, NGC 3201, NGC 6316, and NGC 6440. The paper is organized as follows. In Section 2 we summarize the observations and the adopted data reduction procedures. In Section 3 we discuss the selection of the BSS samples and the measurement of A_{rh}^+ . The discussion of the results and the comparison with other Galactic and extragalactic clusters is presented in Section 4.

2. Observations and Data Reduction

To characterize the BSS distribution in each of the investigated clusters, we took advantage of recent photometric studies performed by our group: Pallanca et al. (2019, 2021) for NGC 6440, Deras et al. (2023) for NGC 6316, Ferraro et al. (2018a) and B. Lanzoni et al. (2023, in preparation) for NGC 3201. In Table 1 we list the main characteristics of the clusters under investigation and the respective reference paper where the photometric data set and the photometric analysis are described in detail. In the following we briefly summarize the relevant information about the adopted data sets and the results of the photometric analyses.

1. *NGC 6440*. The photometric data set consists of a series of deep images of the cluster central regions acquired with the Hubble Space Telescope (HST) Wide Field Camera 3 (WFC3) in different filters (especially the F606W and F814W). To sample the external portion of the system, Pallanca et al. (2021) used a combination of ground-based data acquired with the Focal Reducer/low dispersion Spectrograph2 (FOR2) mounted at the ESO Very Large Telescope, and the Pan-STARRS catalog. The photometric analysis has been carried out by applying the point-spread function (PSF) technique to each exposure. We first modeled the PSF using dozens of bright, isolated, and nonsaturated stars. The model was

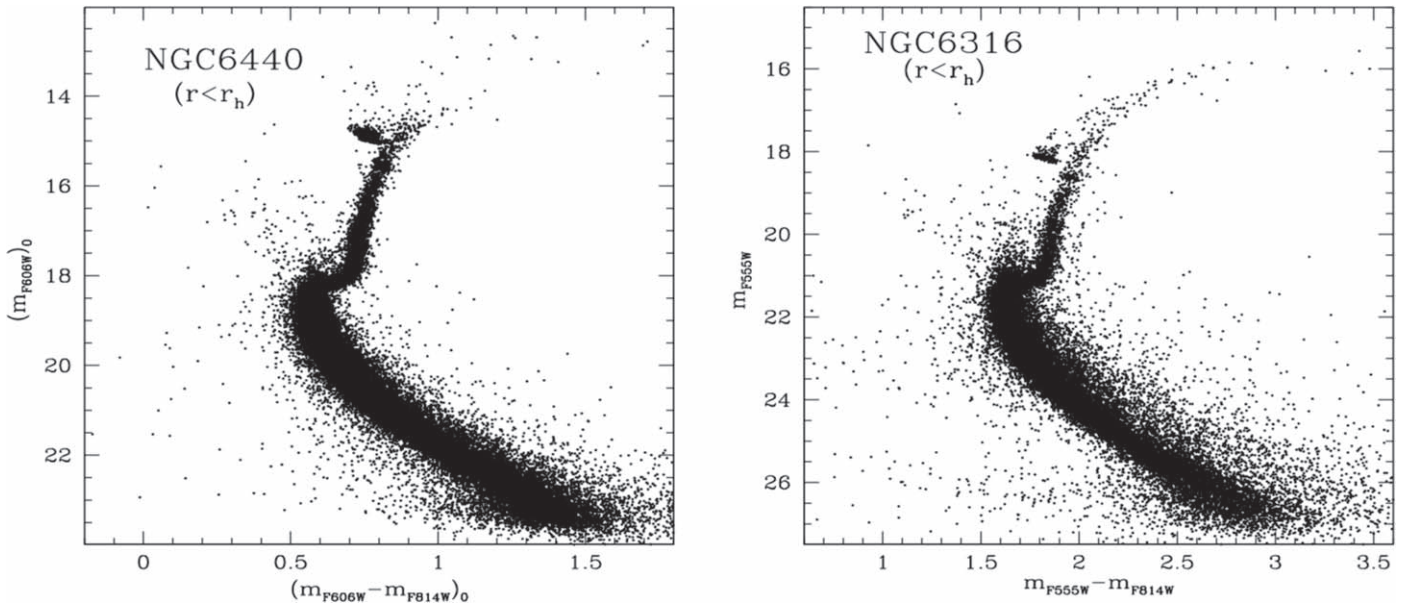


Figure 1. CMDs of NGC 6440 (left) and NGC 6316 (right) within one half-mass radius from the center of each cluster: $r_h = 50''/2$ (Pallanca et al. 2021) and $r_h = 40''$ (Deras et al. 2023), respectively.

Table 1
 A_{rh}^+ Values Determined for the Program Clusters

Cluster	[Fe/H]	r_h	$\lg(l_{rc})$	A_{rh}^+	Reference
NGC 6440	-0.5	50''	7.49	0.30 ± 0.07	Pallanca et al. (2021)
NGC 6316	~ -0.6	40''	8.11	0.24 ± 0.06	Deras et al. (2023)
NGC 3201	-1.6	272''	8.79	0.19 ± 0.07	B. Lanzoni et al. (2023, in preparation)

then applied to all the sources detected at a given level (3σ – 5σ) above the background. We used the DAOPHOT/ALLFRAME package (Stetson 1987, 1994) and followed the standard procedure adopted in many previous papers (see, e.g., Cadelano et al. 2017a, 2019); a photometric catalog listing the frame coordinates and the instrumental magnitudes measured in all the filters for all the detected sources is then obtained. Finally, geometric distortions have been corrected following the prescriptions of Bellini et al. (2011), and the frame coordinates have been reported as R.A. and decl. as defined in the World Coordinate System by using a sample of stars in common with the publicly available Gaia DR2 catalog (Gaia Collaboration et al. 2016a, 2016b). The resulting astrometric accuracy turns out to be better than $\sim 0''.1$. In the case of the HST data, the instrumental magnitudes have been calibrated to the VEGAMAG system by using the reference photometric zero-points reported on the WFC3 website. The available data set allowed Pallanca et al. (2019, 2021) to correct the HST CMD for differential reddening effects, thus providing updated estimates of the cluster age, distance, and absolute reddening. By taking advantage of multi-epoch HST observations, individual proper motions (PMs) have been determined and used to decontaminate the cluster population within $100''$ from the center from field star interlopers. A new identity card of NGC 6440 was thus obtained, with all the structural parameters (such as the core and half-mass radii, the King concentration

parameter, the center of gravity, etc.) being redetermined from its resolved star density profile. Since the main aim of the present paper is to determine the stage of dynamical evolution of each system through measurement of the A_{rh}^+ parameter, in the following we focus our attention on the cluster population included within $r_h = 50.2''$ (Pallanca et al. 2021). The left panel of Figure 1 shows the reddening-corrected and PM-selected CMD of NGC 6440 within one half-mass radius.

2. *NGC 6316.* Deep optical observations obtained with the HST WFC3 in the F555W and the F814W filters have recently been used to analyze the stellar population and the structure of this poorly investigated GC in the Galactic bulge (Deras et al. 2023). The data reduction procedure is very similar to that described above for NGC 6440, and all the details can be found in Deras et al. (2023). Also in this case, a high-resolution extinction map in the direction of the system was determined and used to correct the CMD for the effects of differential reddening. The final CMD extends down to $m_{F555W} = 27$, reaching more than 5 magnitudes below the MS-TO, and it clearly delineates the presence of a metal-rich stellar population, with a well defined red clump and an easily visible red giant branch bump (Fusi Pecci et al. 1990; Ferraro et al. 1999b, 2000; Valenti et al. 2004, 2007). To sample the entire radial extent of the cluster, the HST data (which cover the innermost $\sim 120''$) have been complemented with the Gaia DR3 catalog (Gaia Collaboration et al. 2021). The cluster structural parameters have then

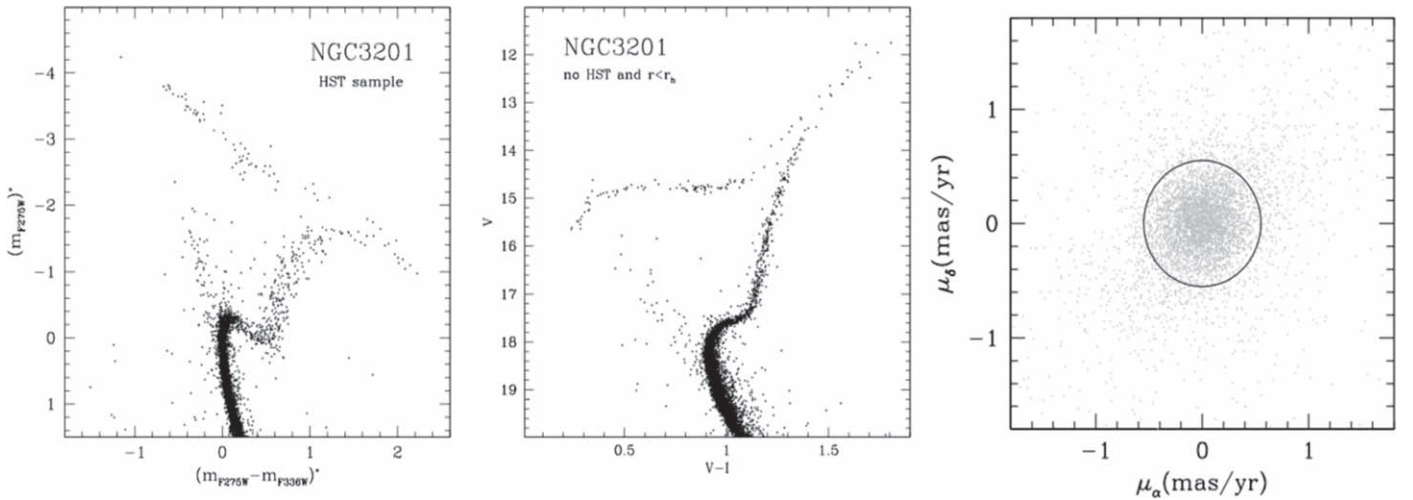


Figure 2. Left: UV CMD of NGC 3201 obtained from HST/WFC3 data sampling the innermost $\sim 100''$ from the center. The observed values of m_{F275} and $(m_{F336W} - m_{F336W})^*$ have been shifted to locate the MS-TO at zero magnitude and color: $(m_{F275})_{\text{MS-TO}}^* = 0$ and $(m_{F336W} - m_{F336W})_{\text{MS-TO}}^* = 0$ (see Ferraro et al. 2018a). Center: differential reddening-corrected optical CMD of NGC 3201 obtained from the Stetson photometric catalog (Stetson et al. 2019) for the stars located beyond the HST/WFC3 field of view and within $r_h = 272''$ (Lanzoni et al. 2023). Only member stars, selected from Gaia PMs as shown in the right panel, are plotted. Right: vector-point diagram for the stars with $V < 19.5$ shown in the central panel. The circle has a radius of 2σ , with σ being the average PM dispersion in the two dimensions. The stars included within the circle are considered to be cluster members and plotted in the central panel.

been determined from the King (1966) model fit to the resolved star density profile. The differential reddening-corrected CMD of NGC 6316 within one half-mass radius ($r_h = 40''$) from the center is shown in the right panel of Figure 1.

3. *NGC 3201.* The central portion of the cluster has been sampled in the context of the HST UV Legacy Survey of GCs (Piotto et al. 2015) through deep WFC3 observations in the F275W and F336W filters. The photometric analysis is described in Ferraro et al. (2018a) and Nardiello et al. (2018). Briefly, for each image we obtained an optimal array of PSFs to properly take into account both the spatial and the temporal PSF variations. To extract the photometric catalogs from each individual exposure by using the adopted arrays of PSFs, we used the software described in Anderson et al. (2008), properly adapted to WFC3 images. As above, the stellar centroids have been corrected for geometric distortion (Bellini et al. 2011) and transformed to the absolute coordinate system, while the instrumental magnitudes have been calibrated to the VEGAMAG system by using the reference photometric zero-points reported on the WFC3 website. The membership probability based on HST PMs has also been determined for each star. This data set has been complemented by a multiband photometric catalog from the Stetson database (Stetson et al. 2019), which samples clustercentric distances out to $\sim 25'$. This has been corrected for differential reddening by following the procedure described in Cadelano et al. (2020c; see also Dalessandro et al. 2018) and then cross-correlated with the Gaia DR3 catalog to select cluster members on the basis of the measured PMs (see the right panel of Figure 2). The resolved star density profile of NGC 3201 has recently been obtained from these data, and the cluster structural parameters have been determined from the best-fit King model to the observed distribution (Lanzoni et al. 2023). Figure 2 shows the PM-selected CMD of the two photometric catalogs used to sample the cluster population within one half-mass radius ($r_h = 272''$).

3. Analysis

3.1. Population Selection

The first step in the measurement of the A_{rh}^+ parameter is the selection of the BSS population in each cluster. As discussed in many previous papers, BSSs are easily recognizable in any CMD independently of the specific filter combination, because they always populate the region that is bluer and brighter than the cluster MS-TO point. To select the BSS population, we followed the procedure adopted in many previous studies over the last 30 years (see, e.g., Ferraro et al. 1992, 1993, 1999a, 2001, 2003, 2006b). In general, we define a selection box as a five-/six-sided polygon aimed at optimizing the separation of BSSs from cluster stars populating the other evolutionary sequences. Typically, the polygon consists of two main lines defining a diagonal strip. Ideally the line that defines the lower diagonal boundary runs close and nearly parallel to the zero-age MS (ZAMS) in that specific filter combination. The upper diagonal boundary is essentially parallel to this first line and it is set to include the bulk of the BSS population. The definition of the bottom edge separating the BSS population from MS-TO and subgiant branch (SGB) stars is somehow the most uncertain and arbitrary. In fact, no sharp separation is theoretically expected between the cluster MS-TO/SGB and the BSS sequence, which merges into the former with no discontinuity. Hence, as a matter of fact, the BSS sequence must be truncated at a given edge. In doing this, we adopt a conservative criterion that naturally takes into account the size of the photometric errors (σ) at the required level of magnitude for the specific program cluster: we define the lower boundary of the BSS selection box at $\sim 4\sigma$ – 5σ from the magnitude and color distribution of the MS-TO/SGB stars. The red boundary of the selection box is generally assumed to follow a vertical line aimed at excluding spurious objects (generally arising from photometric blends) populating the “plume” observed just above the MS-TO. This feature is visible in many CMDs, especially in central regions of high-density clusters, where photometric blends are more probable. Finally, the bright edge of the BSS selection box is needed to distinguish very luminous

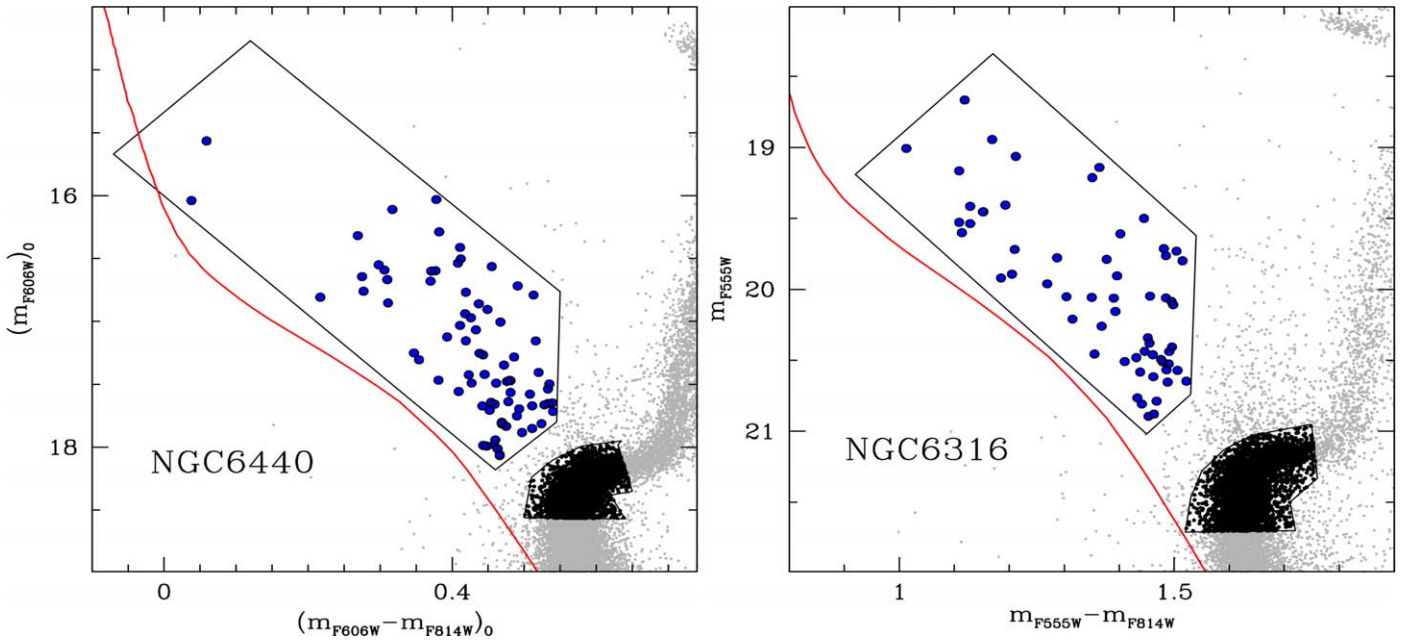


Figure 3. BSS and REF populations (blue and black circles, respectively) selected in NGC 6440 (left) and NGC 6316 (right) within the cluster half-mass radius. The red lines are BaSTI isochrones (Pietrinferni et al. 2006, 2021) with a very young age (40 Myr) representing the ZAMS of each system.

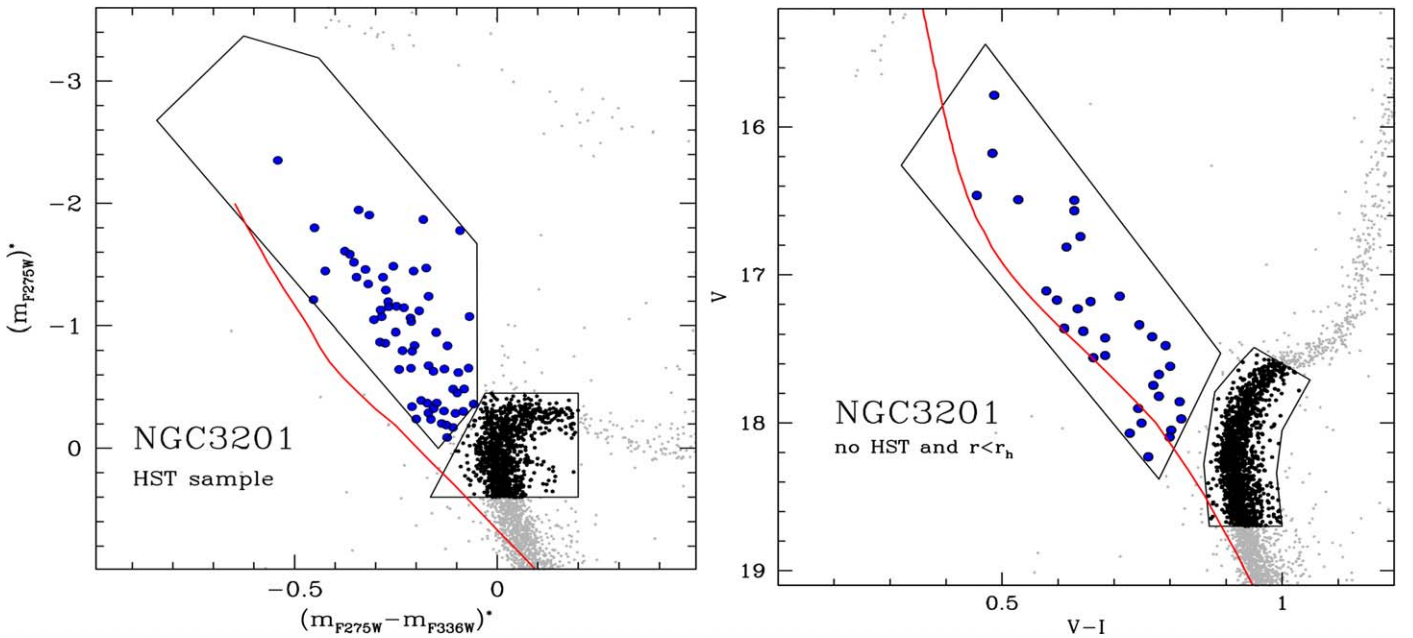


Figure 4. As in Figure 3, but for NGC 3201 in the UV and optical CMDs (left and right panels, respectively) sampling the region included within the cluster half-mass radius ($r_h = 272''$).

BSSs from stars populating the blue portion of the horizontal branch (HB). One or two segments are required depending on the HB morphology and the adopted combination of filters. It is important to emphasize that the inclusion or exclusion of a few “border” objects usually has no or negligible impact on the results.

To determine A_{rh}^+ , the radial distribution of BSSs needs to be compared with that of a REF population of normal (hence, lighter) cluster stars tracing the overall density profile of the system. According to the approach described in Ferraro et al. (2018a), we choose to use as REF the MS stars around the MS-

TO level. Indeed, this is the ideal REF population, because it includes several hundreds to thousands of stars, and therefore is negligibly affected by statistical fluctuations, thus allowing one to maximize the accuracy of the measurement of A_{rh}^+ . Given the intrinsically large statistics of this sample, the inclusion or exclusion of a few objects is even less important than in the case of BSSs. Moreover, since the aim is to trace the radial distribution of “normal” cluster stars, small differences in the shape of the selection boxes are irrelevant. We therefore traced the REF selection boxes with the aim of selecting the bulk of stars in the MS-TO region.

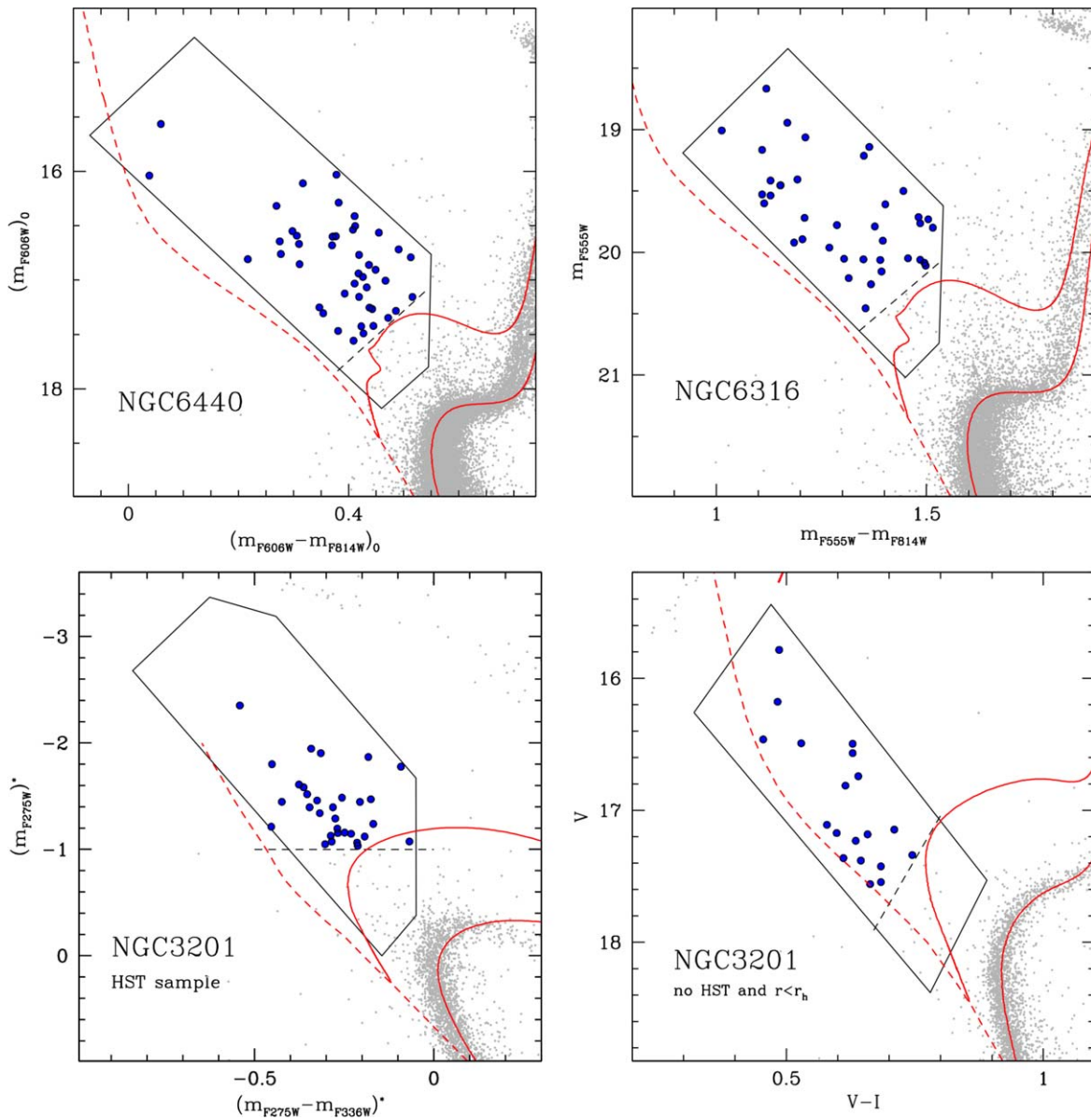


Figure 5. CMDs of the three program clusters with the bright-BSS population (used to compute A_{rh}^{\dagger}) highlighted with large blue circles. In each panel, the rightmost red line is the 12.5 Gyr old BaSTI isochrone (Pietrinferni et al. 2006, 2021) of appropriate metallicity that well reproduces the cluster MS-TO region and has been used to estimate the MS-TO mass. The leftmost red line in each panel is the BaSTI evolutionary track corresponding to a stellar mass $0.2 M_{\odot}$ larger than the MS-TO mass. This has been used to draw the dashed lines in the optical CMDs, above which the bright-BSS samples (large blue circles) have been selected. The BSS selection in the UV CMD (bottom left panel) has been performed as in Ferraro et al. (2018a), at $m_{\text{F275}}^* < -1$, and it corresponds very well to the procedure adopted at optical wavelengths.

Figures 3 and 4 show the adopted selection boxes drawn according to the scheme described above, and the resulting BSS and REF populations in the three program clusters.

3.2. Determination of the A_{rh}^{\dagger} Parameter

Based on the evidence that internal dynamical processes make heavier stars progressively sink toward the center of a cluster more rapidly than less massive ones, the level of central segregation of BSSs with respect to REF stars is a powerful indicator of the stage of dynamical evolution reached by the stellar system. Hence, as discussed in the Introduction, the A_{rh}^{\dagger} parameter has been specifically defined to quantify the level of BSS central segregation in star clusters: it is the area enclosed between the cumulative radial distribution of BSSs and that of a REF population (Alessandrini et al. 2016). To allow

comparison among stellar systems of different intrinsic sizes, the parameter is built by using only the stars included within a fixed physical distance from the cluster center (the half-mass radius). Hence, in building the cumulative radial distributions, the stellar distances from the cluster center are normalized to r_h , and they are expressed in logarithmic units to maximize the sensitivity of the parameter to the innermost regions, where the efficiency of dynamical friction is the highest (see Equation (1) in Lanzoni et al. 2016). Moreover, to further enhance the sensitivity of A_{rh}^{\dagger} to internal dynamical effects, Ferraro et al. (2018a) suggested to consider only the most massive tail of the BSS distribution, by selecting the stars brighter than the MS-TO point in the UV CMD, in particular the BSSs with $m_{\text{F275}}^* < -1$, where m_{F275}^* is the F275W magnitude normalized to the luminosity of the MS-TO of the host cluster (i.e., by

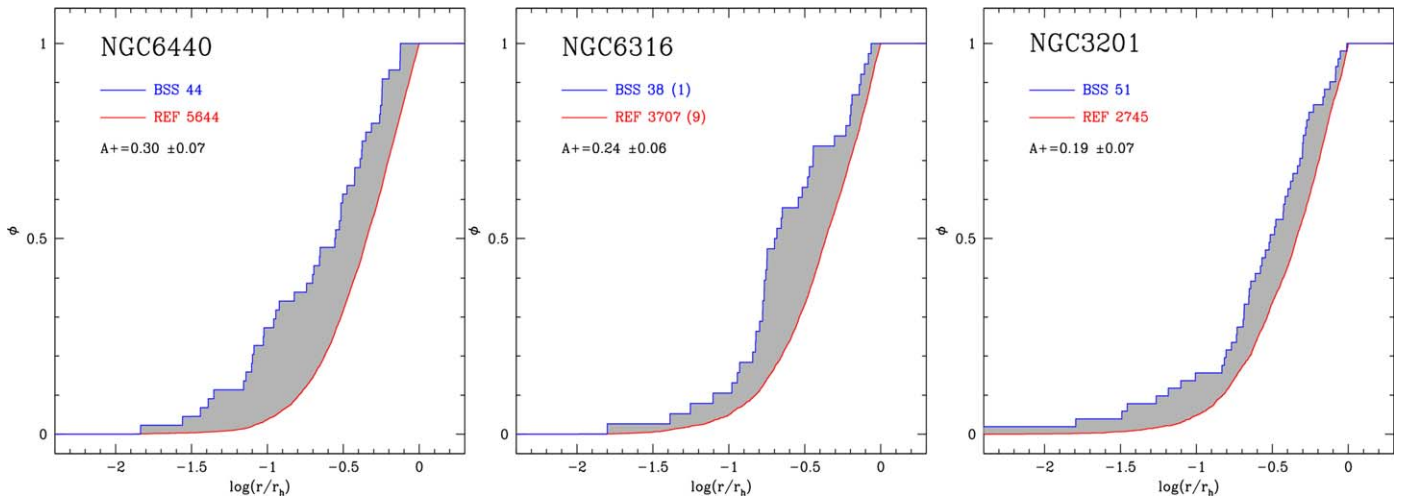


Figure 6. Cumulative radial distributions of BSSs (blue lines) and REF stars (red lines) in the three Galactic GCs discussed in this paper. Only stars within one half-mass radius have been considered and the cumulative radial distributions are therefore normalized to unity at r_h . The size of the area between the two curves (shaded in gray) corresponds to the value of A_{rh}^+ marked in each panel. The number of BSS and REF stars selected in each cluster is given. The number of contaminating field stars is quoted in parenthesis for NGC 6316.

construction, the MS-TO has magnitude $m_{F275W}^* = 0$). Although caution is needed in deriving BSS masses from their luminosity (see Geller & Mathieu 2011), the brightest BSSs are expected to be more massive than the fainter ones. In particular, the adopted threshold in magnitude has been set to select BSSs that are approximately $\Delta m \sim 0.2 M_\odot$ more massive than the MS-TO stars.

To determine the A_{rh}^+ parameter in the three program clusters, we followed the approach described above. First, for the mass selection of BSSs in the UV CMD of NGC 3201, we strictly followed Ferraro et al. (2018a), i.e., we adopted $m_{F275W}^* < -1$ (see the dashed line in the bottom left panel of Figure 5). In all the other cases, when only optical CMDs are available, we used theoretical evolutionary tracks from the BaSTI database (Pietrinferni et al. 2006, 2021) to match the MS-TO region of each system. Since all the three clusters are very old stellar systems, with ages of approximately 12–13 Gyr (Pallanca et al. 2021; Deras et al. 2023), we selected the 12.5 Gyr BaSTI isochrones with the appropriate metallicity. In particular, considering that Galactic GCs typically show α -element enhancements of the order of $[\alpha/Fe] \sim +0.3$, we adopted the BaSTI α -enhanced model with $Z = 1 \times 10^{-3}$ for NGC 3201 (having $[Fe/H] \sim -1.6$; Harris 1996) and with $Z = 8 \times 10^{-3}$ for the two metal-rich systems (NGC 6440 and NGC 6316), where $[Fe/H] \simeq -0.5/-0.6$ (Harris 1996; Origlia et al. 1997, 2008). The adopted isochrones well reproduce the MS-TO region of the three clusters (see the rightmost red lines in each panel of Figure 5), and provide us with the mass of the stars evolving at the MS-TO level: $\sim 0.8 M_\odot$ in the metal-intermediate system NGC 3201, and $\sim 0.9 M_\odot$ in NGC 6440 and NGC 6316. Hence, the threshold adopted to select the bright portion of the BSS distribution (dashed lines in Figure 5) has been set by considering the location of the $1.0 M_\odot$ evolutionary track for NGC 3201, and the $1.1 M_\odot$ model for NGC 6440 and NGC 6316 (leftmost red lines in each panel of the figure). The final samples of selected BSSs are shown as blue circles in Figure 5 and total 50, 44, and 38 objects in NGC 3201, NGC 6440, and NGC 6316, respectively. Their normalized cumulative radial distribution is plotted as a blue line in Figure 6, together with that of the REF population, which is shown in red. The region between the two cumulative

distributions is shaded in gray and its area corresponds to the value of A_{rh}^+ determined in each cluster. It ranges from 0.19 in NGC 3201 to 0.3 in NGC 6440, thus indicating different levels of BSS segregation, corresponding to different levels of internal dynamical evolution. Following Ferraro et al. (2018a), the errors on A_{rh}^+ have been estimated with a jackknife bootstrapping technique (Lupton 1993). In the case of NGC 6316, for which a PM-based membership selection is not feasible yet, we also evaluated the impact on A_{rh}^+ induced by the potential contamination of Galactic field stars in the adopted BSS and REF samples. To this end, we used the Gaia catalog between $500''$ and $600''$ from the center (i.e., well beyond the cluster tidal radius, $r_t = 345''$; Deras et al. 2023) to count the number of field stars that fall within the two selection boxes (see, e.g., Dalessandro et al. 2019). By taking into account the areas covered by this field sample and the area included within the cluster half-mass radius, we estimate that a total of one BSS (out of 38) and nine REF stars (out of 3707) could be field contaminants. We thus performed hundreds of random subtractions (in two separated radial bins) of one and nine stars from the two respective samples, each time recomputing the value of A_{rh}^+ . The result is that field contamination is totally negligible in this cluster. The obtained values of A_{rh}^+ are listed in Table 1, together with those of the half-mass radius, r_h .

3.3. Potential Biases and Uncertainties in the Determination of the A_{rh}^+ Parameter

As discussed in previous papers (e.g., Lanzoni et al. 2016; Ferraro et al. 2018a, 2019), the main sources of possible biases in the determination of the A_{rh}^+ parameter are photometric incompleteness of the samples and severe contamination from field stars. Being stronger in the innermost cluster regions, the effect of incompleteness is to preferentially miss the most central objects. Since field stars essentially have a uniform distribution within the small sky area enclosed by a circle of radius r_h , the effect of field contamination is to “dilute” the radial distribution. Hence, in general both these biases tend to underestimate the value of A_{rh}^+ . This is the reason why we always adopt methodologies specifically designed to reduce,

and possibly eliminate, their impact. Indeed, we always follow the approach of sampling the most crowded central region of the investigated star clusters with high-resolution HST images (acquired in UV or optical filters). Moreover, considering only the brightest portion of the BSS sequence for the measurement of A_{rh}^+ not only maximizes the central sedimentation effect (see Section 3.2) but also reduces the impact of incompleteness. This is also supported by the artificial star experiments, which confirm the high level (>90%) of photometric completeness for the adopted BSS samples. To minimize/avoid the potential bias introduced by field star contamination, we used PM-selected samples in most of the cases. When PMs are not available (e.g., for NGC 6316 and the GCs in the LMC), a statistical decontamination of the samples has been performed by evaluating the number of potential field stars, running hundreds of random subtractions of them from the selected BSS populations, and thus including this effect in the overall uncertainty of the measurement.

Once incompleteness and field contamination are under control, the primary source of uncertainty on A_{rh}^+ remains the relatively small number statistics of the BSS sample. As mentioned above, to estimate the errors on A_{rh}^+ we adopted a jackknife bootstrapping technique (Lupton 1993): operatively, for a sample of N BSSs, we determined the value of A_{rh}^+ N times by using samples of $(N - 1)$ BSSs obtained by excluding, each time, one different star. Thus, the procedure yields N estimates of the parameter and the final uncertainty on A_{rh}^+ is obtained as $\sigma_{A^+} = \sigma_{\text{distr}} \times \sqrt{N - 1}$, where σ_{distr} is the standard deviation of the A_{rh}^+ distribution derived from the N realizations.

4. Discussion

The values of A_{rh}^+ determined here for the three program clusters can now be compared with those obtained in previous studies through a similar methodology. Following Ferraro et al. (2018a), the comparison is worth doing in a diagram that relates the values of A_{rh}^+ to the number of present-day central relaxation times suffered by each system since the epoch of its formation (N_{relax}). The value of N_{relax} can be derived by simply dividing the age of the cluster⁴ by its central relaxation time, estimated from the well-known expression (Spitzer 1987; Djorgovski 1993):

$$t_{\text{rc}} = 8.338 \times 10^6 \times \ln(0.4N_*)^{-1} \rho_0^{1/2} m_*^{-1} r_c^3, \quad (1)$$

where N_* is the total number of stars, computed as the ratio between the total cluster mass (M_{tot}) and the average stellar mass (here we adopt $m_* = 0.3 M_{\odot}$), ρ_0 is the central mass density in units of $M_{\odot} \text{pc}^{-3}$, determined through Equation (7) in Djorgovski (1993), and r_c is the core radius in parsecs. In turn, M_{tot} is obtained from the product of the absolute V -band magnitude of the cluster (M_V) listed in the Harris (1996) catalog and the V -band mass-to-light ratio appropriate for old stellar systems ($M/L_V = 2$; e.g., Maraston 1998). Figure 7 compares the values of $\log(N_{\text{relax}})$ versus A_{rh}^+ obtained for the three clusters analyzed here (large red squares) with those previously measured in a consistent way for other systems, namely, the 48 Galactic GCs presented in Ferraro et al. (2018a) and NGC 6256 from Cadelano et al. (2022, gray circles), five old clusters in the

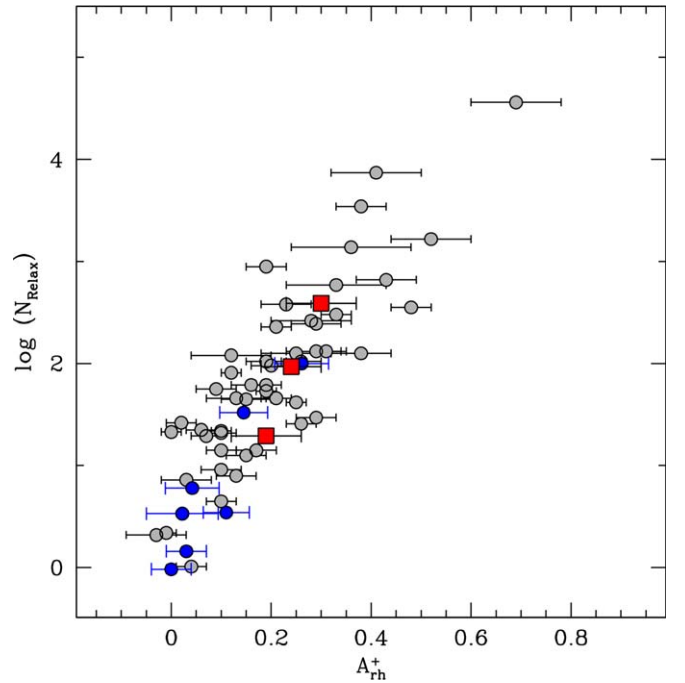


Figure 7. Correlation between the BSS segregation level (measured by the A_{rh}^+ parameter) and the number of current central relaxation times that have elapsed since cluster formation (N_{relax}) in the sample of star clusters analyzed so far: the three systems studied here are highlighted with large red squares, and the 48 Galactic GCs discussed in Ferraro et al. (2018a) and the cluster (NGC 6256) studied in Cadelano et al. (2022) are plotted as gray circles, while the five LMC and two SMC clusters presented in Ferraro et al. (2019) and Dresbach et al. (2022), respectively, are marked with blue circles.

LMC, and two young SMC clusters discussed, respectively, in Ferraro et al. (2019) and Dresbach et al. (2022, blue circles). Considering the three systems studied here, a grand total of 59 stellar clusters have been investigated so far in different environments. As is apparent from Figure 7, they draw a well defined relation between A_{rh}^+ and N_{relax} , thus proving and consolidating the use of the dynamical clock as a powerful method to track the dynamical evolution of stellar systems, and the use of A_{rh}^+ as a sensitive clock-hand to rank star clusters in terms of their dynamical age, irrespective of the host environment.

The tight relation shown in Figure 7 indicates that A_{rh}^+ and N_{relax} both provide a measure of the dynamical aging of stellar systems. However, it is worth adding a few considerations about the two indicators. The dynamical evolution of a cluster is driven by the complex combination of effects associated with a variety of internal and external properties and dynamical processes (e.g., two-body relaxation, interactions with the Galactic tidal field along the cluster orbit, initial structural and kinematic properties of the cluster, and its stellar content; see, e.g., Heggie & Hut 2003). The value of t_{rc} provides a measure of the present-day central relaxation timescale and it is based on a simple analytical expression derived under the assumption of spherical symmetry and isotropic and nonrotating internal kinematics. However, recent observational investigations (e.g., Fabricius et al. 2014; Watkins et al. 2015; Bellini et al. 2017; Lanzoni et al. 2018a, 2018b; Ferraro et al. 2018b; Kamann et al. 2018; Leanza et al. 2022) have revealed that some GCs are characterized by internal rotation and velocity anisotropy,

⁴ In accord with Ferraro et al. (2018a) we adopted 12 Gyr as the average age for GGCs; see the compilation by Forbes & Bridges (2010).

and several theoretical studies have shown that these kinematic properties have a significant effect on all the aspects of the dynamical evolution of GCs (see, e.g., Kim et al. 2004; Hong et al. 2013; Breen et al. 2017; Tiongco et al. 2017; Pavlík & Vesperini 2021, 2022a, 2022b; Kamlah et al. 2022; Livernois et al. 2022). In addition, depending on the central density, core radius, and total mass, the value of t_{rc} computed through Equation (1) varies during cluster dynamical evolution. Hence, the present-day value of t_{rc} may fail to provide a complete picture of the past evolutionary history of a system. In fact, by construction, two clusters with similar present-day structural properties would share the same value of t_{rc} , even though they experienced different dynamical evolutionary histories. Hence, using this value as an estimate of the systems' dynamical age may not capture differences in their past evolution. On the observational side it is also worth mentioning the large uncertainties in the derivation of reliable estimates of t_{rc} in the case of post-core-collapse (PCC) clusters, where the presence of an inner cusp in the star density/surface brightness profile allows no proper fit with the King model family, and therefore prevents any reasonable measurement of r_c (and possibly invalidates its meaning itself). Indeed, the difficulty in determining the structural parameters of PCC clusters is possibly at the origin of the large spread of t_{rc} (hence, N_{relax}) values in the most advanced stages of dynamical evolution (see the top right corner of Figure 7). On the other hand, by leveraging the observed spatial concentration of the BSS populations, A_{rh}^+ provides a direct empirical measurement of the degree of mass segregation developed during the *entire* cluster's evolution. In addition, such an observational measurement does not rely on simplifying assumptions and approximations, and represents a more direct indicator of the cluster's dynamical history than the present-day value of t_{rc} .

A few cases provides interesting examples of how the A_{rh}^+ parameter may reveal a more detailed picture of the dynamical history of globular clusters. NGC 4590 and M3 (NGC 5272) have the same relaxation time ($\sim 4.6 \times 10^8$ yr) but very distinct values of A_{rh}^+ : 0.02 and 0.26, respectively. The latter clearly shows that M3 is dynamically much older than NGC 4590, which is consistent with its more compact structure and higher central density. Similarly, the dynamical clock indicates that, in spite of the same relaxation time ($t_{rc} \simeq 3.1 \times 10^7$ yr), NGC 6440 ($A_{rh}^+ = 0.30$) is more dynamically evolved than NGC 6535 ($A_{rh}^+ = 0.23$), which is a significantly less compact and less massive cluster. Note that the high dynamical activity in the core of NGC 6440 is also attested to by the presence of a significant population of millisecond pulsars (MSPs): eight MSPs have been found so far in this stellar system (see Freire et al. 2008; Vleschower et al. 2022). More intriguingly, NGC 6440 is one of the three Galactic GCs (beside M28 and NGC 2808) hosting a so-called accreting millisecond X-ray pulsar, a subgroup of transient low-mass X-ray binaries that show, during outbursts, X-ray pulsations from a rapidly rotating neutron star (see Sanna et al. 2016; Cadelano et al. 2017a). The object in NGC 6440 is characterized by an ongoing mass transfer process that, according to the currently accepted recycling formation scenario (Bhattacharya & van den Heuvel 1991), will yield the appearance of a newborn MSP (see Ferraro et al. 2015) in the radio band as soon as the radio signal is reactivated. This, together with the high BSS sedimentation level attested to by the measured value of A_{rh}^+ , can be considered as a clear signature of intense dynamical

activity occurring in the core of a cluster on the verge of CC. A deeper investigation of these cases can provide illuminating details on the processes that contribute to determining the dynamical aging of star clusters.

As quoted above, Figure 7 also includes seven clusters in the LMC and SMC with old and intermediate chronological ages, respectively, which have been found to span values of A_{rh}^+ between 0 and 0.26 (blue circles in the figure). It would now be valuable to extend the measurement to the PCC clusters of the LMC, thus probing the entire range of dynamical ages sampled by $A_{rh}^+ - N_{relax}$ relation in extragalactic context. However, the nice way in which the LMC and SMC clusters merge into the Milky Way relation suggests that this holds also in external galaxies. In particular, the old LMC clusters NGC 2210, NGC 2257, and Hodge 11 turn out to essentially share the same dynamical ages (and similar structural parameters) as the Milky Way GCs M92 (NGC 6341), NGC 5466, and NGC 6101, respectively. In addition, the null value of A_{rh}^+ (indicating that BSSs have yet to start their central sedimentation) that has been measured in the intermediate–young SMC clusters NGC 339 and NGC 419 is comparable to that observed in three old GCs in the Milky Way (namely, ω Centauri, NGC 2419, and Palomar 14) and in two old GCs in the LMC (NGC 1841 and Hodge 11). This evidence strongly suggests that a lack of BSS segregation (i.e., a BSS radial distribution indistinguishable from that of lighter stars) can be reasonably read as the *initial* condition of any cluster, before internal dynamical processes start to significantly modify the spatial distribution of stellar masses and the overall structure of the system. Hence, the large core radius measured in various old clusters of the LMC can just correspond to the initial conditions at the moment of formation (see Ferraro et al. 2019), instead of being the result of a core expansion due to the action of a binary black hole population (as suggested by Mackey et al. 2008).

Interestingly, the seven Galactic GCs in the surveyed sample that are classified as PCC systems in the Harris (1996) catalog (namely, M15, M30, M70, NGC 6397, NGC 6624, NGC 6256, and NGC 6752) all have $A_{rh}^+ \geq 0.29$, and the same holds for NGC 362, which is a suspected PCC system in the Harris (1996) catalog and confirmed to be so in Dalessandro et al. (2013): they are plotted as large red triangles in Figure 8. This evidence provides a series of additional considerations on the potential information provided by the dynamical clock. In fact $A_{rh}^+ \sim 0.30$ (dashed line in the figure) can be considered a sort of reference value for the CC event, meaning that the proximity of A_{rh}^+ to this value is likely an indication of the imminence of CC. In this respect, GCs such as NGC 6440, NGC 6229, and 47 Tucanae (with $A_{rh}^+ = 0.29$ – 0.30) should be very close to CC. Very intriguing cases are the four clusters (namely M80, M75, NGC 6652, and NGC 1851) showing $A_{rh}^+ > 0.33$ and no evidence (at least known so far) of a steep cusp in the innermost portion of the star density/brightness profile, which is considered to be the typical signature of CC. These clusters are surely worth deeper investigations to confirm that they show no signatures of CC. If they do not, the large values A_{rh}^+ could be interpreted as the manifestation of a population of collisional and mass-transfer BSSs generated in the core by an increased rate of binary interactions that are contributing to delaying CC. In this case, other signatures of this activity should also be detectable since compact binaries forming and hardening in the core can manifest themselves as interacting binaries. Intriguingly, a high rate of ongoing dynamical

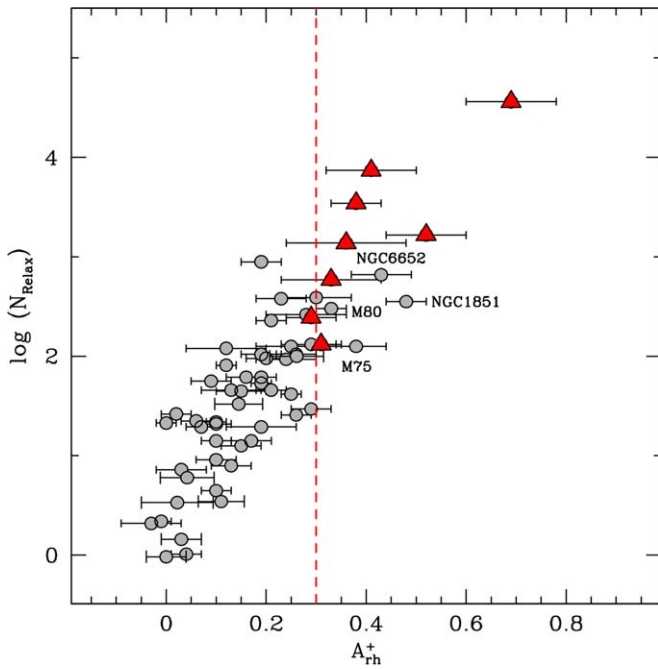


Figure 8. Same as in Figure 7, with the position of the eight confirmed PCC clusters highlighted with large red triangles. The vertical dashed line at $A_{rh}^+ = 0.30$ likely flags the reference value of A_{rh}^+ for the occurrence of CC. The four clusters with $A_{rh}^+ > 0.30$ but no clear evidence of CC based on the shape of their density profile is labeled.

interactions in the cores of NGC 1851 and NGC 6652 is suggested by the presence of recently formed MSPs, possibly generated by exchange interactions (Ridolfi et al. 2022 and Chen et al. 2023, respectively). On the other hand, the large range of values of A_{rh}^+ found for PCC clusters (from ~ 0.3 to ~ 0.7) suggests that an intense and progressive growth of the BSS population in the cluster center takes place also during the PCC stage, again possibly tracing an increased formation of these stars due to stellar collisions and enhanced mass transfer activity in (hard) binaries. Interestingly enough, a possible confirmation of this activity arrives from the analysis of the rotational velocity of BSSs in PCC clusters (see Figure 3 in Ferraro et al. 2023). In fact, the fraction of fast spinning BSSs (which is a signature of recent formation; Sills et al. 2005; Leiner et al. 2018) shows a (mild) increase with A_{rh}^+ , which might indicate that the dynamical activity occurring during the recurrent re-contractions of the cluster core in the PCC evolutionary stage could favor the formation of these stars.

All the considerations above support the importance of the dynamical clock and further sustain its potential use in the near future as a powerful indicator of dynamical evolution. In fact, the upcoming generation of telescopes will open the exploration of resolved populations in star clusters in external galaxies, allowing a straightforward selection of BSSs and the study of their radial distribution. Indeed, the observational capabilities of the JWST have already extended the exploration of resolved stellar populations below the MS-TO level in the GC systems of the entire Local Group, including the populous systems in the Andromeda galaxy, in M33, and in many nearby dwarf galaxies. This exploration will be further pushed forward by the Multi-AO Imaging Camera for Deep Observations (MICADO) that will be mounted at the ESO Extremely Large Telescope (a telescope with a 39 m primary mirror) and will provide a spatial resolution a factor of 6 better than the JWST. Indeed, for these

distant systems, the A_{rh}^+ parameter will effectively be the easiest (if not the only) diagnostic available to study their dynamical stage. In turn, this will promote a variety of science cases, allowing, e.g., the appropriate selection of dynamically old clusters on the verge of CC, the identification of dynamically young systems in which to study the initial conditions of their (possibly multiple) populations, and even the study of the effects that the interaction with the parent galaxy may have on the dynamical aging of star clusters.

Acknowledgments

This work is part of the project Cosmic-Lab (Globular Clusters as Cosmic Laboratories) at the Physics and Astronomy Department “A. Righi” of the Bologna University (<http://www.cosmic-lab.eu/Cosmic-Lab/Home.html>). The research was funded by the MIUR throughout the PRIN-2017 grant awarded to the project Light-on-Dark (PI: Ferraro) through contract PRIN-2017K7REXT.

ORCID iDs


Francesco R. Ferraro  <https://orcid.org/0000-0002-2165-8528>

Barbara Lanzoni  <https://orcid.org/0000-0001-5613-4938>

Enrico Vesperini  <https://orcid.org/0000-0003-2742-6872>

Mario Cadelano  <https://orcid.org/0000-0002-5038-3914>

Dan Deras  <https://orcid.org/0000-0002-3730-9664>

Cristina Pallanca  <https://orcid.org/0000-0002-7104-2107>

References

- Alessandrini, E., Lanzoni, B., Ferraro, F. R., et al. 2016, *ApJ*, 833, 252
 Anderson, J., Sarajedini, A., Bedin, L. R., et al. 2008, *AJ*, 135, 2055
 Baumgardt, H., & Makino, J. 2003, *MNRAS*, 340, 227
 Beccari, G., Cadelano, M., & Dalessandro, E. 2023, *A&A*, 670, A11
 Beccari, G., Ferraro, F. R., Dalessandro, E., et al. 2019, *ApJ*, 876, 87
 Beccari, G., Sollima, A., Ferraro, F. R., et al. 2011, *ApJL*, 737, L3
 Bellini, A., Anderson, J., & Bedin, L. R. 2011, *PASP*, 123, 622
 Bellini, A., Bianchini, P., Varri, A. L., et al. 2017, *ApJ*, 844, 167
 Bhat, B., Lanzoni, B., Ferraro, F. R., et al. 2022, *ApJ*, 926, 118
 Bhattacharya, D., & van den Heuvel, E. P. J. 1991, *PhR*, 203, 1
 Bianchini, P., van de Ven, G., Norris, M. A., et al. 2016, *MNRAS*, 458, 3644
 Bianchini, P., van der Marel, R. P., del Pino, A., et al. 2018, *MNRAS*, 481, 2125
 Breen, P. G., Varri, A. L., & Heggie, D. C. 2017, *MNRAS*, 471, 2778
 Cadelano, M., Chen, J., Pallanca, C., et al. 2020b, *ApJ*, 905, 63
 Cadelano, M., Dalessandro, E., Ferraro, F. R., et al. 2017b, *ApJ*, 836, 170
 Cadelano, M., Dalessandro, E., Webb, J. J., et al. 2020a, *MNRAS*, 499, 2390
 Cadelano, M., Ferraro, F. R., Dalessandro, E., et al. 2022, *ApJ*, 941, 69
 Cadelano, M., Ferraro, F. R., Istrate, A. G., et al. 2019, *ApJ*, 875, 25
 Cadelano, M., Pallanca, C., Ferraro, F. R., et al. 2017a, *ApJ*, 844, 53
 Cadelano, M., Saracino, S., Dalessandro, E., et al. 2020c, *ApJ*, 895, 54
 Cadelano, M., Ransom, S. M., Freire, P. C. C., et al. 2018, *ApJ*, 855, 125
 Chen, J., Cadelano, M., Pallanca, C., et al. 2023, *ApJ*, 948, 84
 Cohen, R. E., Bellini, A., Libralato, M., et al. 2021, *AJ*, 161, 41
 Dalessandro, E., Ferraro, F. R., Bastian, N., et al. 2019, *A&A*, 621, A45
 Dalessandro, E., Ferraro, F. R., Massari, D., et al. 2013, *ApJ*, 778, 135
 Dalessandro, E., Lanzoni, B., Ferraro, F. R., et al. 2008, *ApJ*, 681, 311
 Dalessandro, E., Lardo, C., Cadelano, M., et al. 2018, *A&A*, 618, A131
 Deras, D., Cadelano, M., Ferraro, F. R., et al. 2023, *ApJ*, 942, 104
 Djorgovski, S. 1993, in ASP Conf. Ser. 50, Structure and Dynamics of Globular Clusters, ed. G. Djorgovski & G. Meylan (San Francisco, CA: ASP)
 Dresbach, F., Massari, D., Lanzoni, B., et al. 2022, *ApJ*, 928, 47
 Fabricius, M. H., Noyola, E., Rukdee, S., et al. 2014, *ApJL*, 787, L26
 Ferraro, F. R., Beccari, G., Dalessandro, E., et al. 2009, *Natur*, 462, 1028
 Ferraro, F. R., Fusi Pecci, F., & Buonanno, R. 1992, *MNRAS*, 256, 376
 Ferraro, F. R., Lanzoni, B., & Dalessandro, E. 2020, *PLSFRN*, 31, 19
 Ferraro, F. R., Lanzoni, B., Dalessandro, E., et al. 2012, *Natur*, 492, 393
 Ferraro, F. R., Lanzoni, B., Dalessandro, E., et al. 2019, *NatAs*, 3, 1149

- Ferraro, F. R., Lanzoni, B., Raso, S., et al. 2018a, *ApJ*, **860**, 36
- Ferraro, F. R., Messineo, M., Fusi Pecci, F., et al. 1999b, *AJ*, **118**, 1738
- Ferraro, F. R., Montegriffo, P., Origlia, L., et al. 2000, *AJ*, **119**, 1282
- Ferraro, F. R., Mucciarelli, A., Lanzoni, B., et al. 2018b, *ApJ*, **860**, 50
- Ferraro, F. R., Mucciarelli, A., Lanzoni, B., et al. 2023, *NatCo*, in press
- Ferraro, F. R., Pallanca, C., Lanzoni, B., et al. 2015, *ApJL*, **807**, L1
- Ferraro, F. R., Pallanca, C., Lanzoni, B., et al. 2021, *NatAs*, **5**, 311
- Ferraro, F. R., Paltrinieri, B., Fusi Pecci, F., et al. 1997, *A&A*, **324**, 915
- Ferraro, F. R., Paltrinieri, B., Rood, R. T., et al. 1999a, *ApJ*, **522**, 983
- Ferraro, F. R., Pecci, F. F., Cacciari, C., et al. 1993, *AJ*, **106**, 2324
- Ferraro, F. R., Possenti, A., D'Amico, N., et al. 2001, *ApJL*, **561**, L93
- Ferraro, F. R., Sabbi, E., Gratton, R., et al. 2006a, *ApJL*, **647**, L53
- Ferraro, F. R., Sollima, A., Rood, R. T., et al. 2006b, *ApJ*, **638**, 433
- Ferraro, F. R., Sills, A., Rood, R. T., et al. 2003, *ApJ*, **588**, 464
- Fiorentino, G., Lanzoni, B., Dalessandro, E., et al. 2014, *ApJ*, **783**, 34
- Forbes, D. A., & Bridges, T. 2010, *MNRAS*, **404**, 1203
- Freire, P. C. C., Ransom, S. M., Bégin, S., et al. 2008, *ApJ*, **675**, 670
- Fusi Pecci, F., Ferraro, F. R., Crocker, D. A., et al. 1990, *A&A*, **238**, 95
- Gaia Collaboration, Brown, A. G. A., Vallenari, A., et al. 2016a, *A&A*, **595**, A2
- Gaia Collaboration, Brown, A. G. A., Vallenari, A., et al. 2021, *A&A*, **649**, A1
- Gaia Collaboration, Prusti, T., de Bruijne, J. H. J., et al. 2016b, *A&A*, **595**, A1
- Geller, A. M., & Mathieu, R. D. 2011, *Natur*, **478**, 356
- Gilliland, R. L., Bono, G., Edmonds, P. D., et al. 1998, *ApJ*, **507**, 818
- Harris, W. E. 1996, *AJ*, **112**, 1487
- Heggie, D., & Hut, P. 2003, *The Gravitational Million-Body Problem* (Cambridge: Cambridge Univ. Press)
- Hills, J. G., & Dale, T. M. 1974, *A&A*, **30**, 135
- Hong, J., Kim, E., Lee, H. M., et al. 2013, *MNRAS*, **430**, 2960
- Kamann, S., Husser, T.-O., Dreizler, S., et al. 2018, *MNRAS*, **473**, 5591
- Kamlah, A. W. H., Spurzem, R., Berczik, P., et al. 2022, *MNRAS*, **516**, 3266
- Kim, E., Lee, H. M., & Spurzem, R. 2004, *MNRAS*, **351**, 220
- King, I. R. 1966, *AJ*, **71**, 64
- Lanzoni, B., Dalessandro, E., Ferraro, F. R., et al. 2007a, *ApJL*, **668**, L139
- Lanzoni, B., Dalessandro, E., Perina, S., et al. 2007b, *ApJ*, **670**, 1065
- Lanzoni, B., Ferraro, F. R., Alessandrini, E., et al. 2016, *ApJL*, **833**, L29
- Lanzoni, B., Ferraro, F. R., Dalessandro, E., et al. 2010, *ApJ*, **717**, 653
- Lanzoni, B., Ferraro, F. R., Dalessandro, E., et al. 2019, *ApJ*, **887**, 176
- Lanzoni, B., Ferraro, F. R., Mucciarelli, A., et al. 2018a, *ApJ*, **861**, 16
- Lanzoni, B., Ferraro, F. R., Mucciarelli, A., et al. 2018b, *ApJ*, **865**, 11
- Lanzoni, B., Mucciarelli, A., Origlia, L., et al. 2013, *ApJ*, **769**, 107
- Lanzoni, B., Sanna, N., Ferraro, F. R., et al. 2007c, *ApJ*, **663**, 1040
- Leanza, S., Pallanca, C., Ferraro, F. R., et al. 2022, *ApJ*, **929**, 186
- Leigh, N., Sills, A., & Knigge, C. 2007, *ApJ*, **661**, 210
- Leiner, E., Mathieu, R. D., Gosnell, N. M., et al. 2018, *ApJL*, **869**, L29
- Libralato, M., Bellini, A., Piotto, G., et al. 2019, *ApJ*, **873**, 109
- Libralato, M., Bellini, A., van der Marel, R. P., et al. 2018, *ApJ*, **861**, 99
- Livernois, A. R., Vesperini, E., Varri, A. L., et al. 2022, *MNRAS*, **512**, 2584
- Lupton, R. 1993, *Statistics in Theory and Practice* (Princeton, NJ: Princeton Univ. Press)
- Mackey, A. D., & Gilmore, G. F. 2003a, *MNRAS*, **338**, 85
- Mackey, A. D., & Gilmore, G. F. 2003b, *MNRAS*, **338**, 120
- Mackey, A. D., Wilkinson, M. I., Davies, M. B., et al. 2008, *MNRAS*, **386**, 65
- Maraston, C. 1998, *MNRAS*, **300**, 872
- McCrea, W. H. 1964, *MNRAS*, **128**, 147
- Meylan, G., & Heggie, D. C. 1997, *A&ARv*, **8**, 1
- Miocchi, P., Lanzoni, B., Ferraro, F. R., et al. 2013, *ApJ*, **774**, 151
- Moretti, A., de Angeli, F., & Piotto, G. 2008, *A&A*, **483**, 183
- Nardiello, D., Libralato, M., Piotto, G., et al. 2018, *MNRAS*, **481**, 3382
- Origlia, L., Ferraro, F. R., Fusi Pecci, F., et al. 1997, *A&A*, **321**, 859
- Origlia, L., Valenti, E., & Rich, R. M. 2008, *MNRAS*, **388**, 1419
- Pallanca, C., Ferraro, F. R., Lanzoni, B., et al. 2019, *ApJ*, **882**, 159
- Pallanca, C., Lanzoni, B., Ferraro, F. R., et al. 2021, *ApJ*, **913**, 137
- Pavlík, V., & Vesperini, E. 2021, *MNRAS Lett.*, **504**, L12
- Pavlík, V., & Vesperini, E. 2022a, *MNRAS*, **509**, 3815
- Pavlík, V., & Vesperini, E. 2022b, *MNRAS*, **515**, 1830
- Pietrinferni, A., Cassisi, S., Salaris, M., et al. 2006, *ApJ*, **642**, 797
- Pietrinferni, A., Hidalgo, S., Cassisi, S., et al. 2021, *ApJ*, **908**, 102
- Piotto, G., De Angeli, F., King, I. R., et al. 2004, *ApJL*, **604**, L109
- Piotto, G., Milone, A. P., Bedin, L. R., et al. 2015, *AJ*, **149**, 91
- Poolley, D., Lewin, W. H. G., Anderson, S. F., et al. 2003, *ApJL*, **591**, L131
- Prager, B. J., Ransom, S. M., Freire, P. C. C., et al. 2017, *ApJ*, **845**, 148
- Ransom, S. M., Hessels, J. W. T., Stairs, I. H., et al. 2005, *Sci*, **307**, 892
- Raso, S., Libralato, M., Bellini, A., et al. 2020, *ApJ*, **895**, 15
- Raso, S., Pallanca, C., Ferraro, F. R., et al. 2019, *ApJ*, **879**, 56
- Ridolfi, A., Freire, P. C. C., Gautam, T., et al. 2022, *A&A*, **664**, A27
- Sandage, A. R. 1953, *AJ*, **58**, 61
- Sanna, A., Burderi, L., Riggio, A., et al. 2016, *MNRAS*, **459**, 1340
- Shara, M. M., Saffer, R. A., & Livio, M. 1997, *ApJL*, **489**, L59
- Sills, A., Adams, T., & Davies, M. B. 2005, *MNRAS*, **358**, 716
- Simunovic, M., & Puzia, T. H. 2016, *MNRAS*, **462**, 3401
- Spitzer, L. 1987, *Dynamical Evolution of Globular Clusters* (Princeton, NJ: Princeton Univ. Press)
- Stetson, P. B. 1987, *PASP*, **99**, 191
- Stetson, P. B. 1994, *PASP*, **106**, 250
- Stetson, P. B., Pancino, E., Zocchi, A., et al. 2019, *MNRAS*, **485**, 3042
- Tiongco, M. A., Vesperini, E., & Varri, A. L. 2016, *MNRAS*, **455**, 3693
- Tiongco, M. A., Vesperini, E., & Varri, A. L. 2017, *MNRAS*, **469**, 683
- Trenti, M., & van der Marel, R. 2013, *MNRAS*, **435**, 3272
- Valenti, E., Ferraro, F. R., & Origlia, L. 2004, *MNRAS*, **351**, 1204
- Valenti, E., Ferraro, F. R., & Origlia, L. 2007, *AJ*, **133**, 1287
- Verbunt, F., & Freire, P. C. C. 2014, *A&A*, **561**, A11
- Vleeschower, L., Stappers, B. W., Bailes, M., et al. 2022, *MNRAS*, **513**, 1386
- Watkins, L. L., van der Marel, R. P., Bellini, A., et al. 2015, *ApJ*, **803**, 29
- Webb, J. J., & Vesperini, E. 2017, *MNRAS*, **464**, 1977